Probing Wigner time delays with photoelectron interferometry: Anisotropic long-range imprint of the short-range centrifugal potential

Morgan Berkane, Camille Lévêque, Richard Taïeb,* Jérémie Caillat, and Jonathan Dubois
Sorbonne Université, CNRS, Laboratoire de Chimie Physique-Matière et Rayonnement, LCPMR, F-75005 Paris, France

(Received 16 May 2024; accepted 1 July 2024; published 22 July 2024)

We consider the comparative dynamics of one- and two-photon ionization in atoms through semianalytical representations of the continuum wave functions, in order to model the probe-induced anisotropy in interferometric measurements of photoemission delays. We find an approximate expression of the long-range half-scattering phase based on an asymptotic expansion of the continuum eigenfunctions within the Wentzel-Kramers-Brillouin approximation, which encompasses and expands commonly used lower-order derivations. Combined with a perturbative approach, the resulting analytic formalism can treat, at the same time, the two-photon propensity rules, the anisotropy in the continuum-continuum photoionization time delay, and the soft-photon regime.

DOI: 10.1103/PhysRevA.110.013120

I. INTRODUCTION

Attosecond spectroscopies rely to a large extent on interferometric schemes, due to the extremely short timescale and the wavelike nature of the investigated quantum processes [1,2]. In particular, two pillars of attosecond science, i.e., the attosecond streaking [3] and the reconstruction of attosecond beating by interference of two-photon transitions (RABBIT) [4] techniques, have been used to revisit photoemission in the time domain [5–7].

The attosecond streaking and RABBIT are schemes based on two-photon ionization with extreme ultraviolet (XUV) attosecond pulses dressed with an infrared (IR) field. Using them as XUV-pump IR-probe approaches to gain temporal insight into photoemission from atoms [6,7], through measurements of the photoelectron's spectral phase, triggered intense experimental and theoretical activities (see, e.g., Ref. [8] and references therein). A major issue addressed in this context concerns the intricate roles of the XUV pump and the IR probe and more specifically the imprint of the latter on the measured photoemission delays. Analytical derivations based on universal asymptotic expansions of the wave functions [6,7,9] and classical arguments [10–14] have proved efficient for the modeling and interpretation in various studies over the past decade (see, e.g., Refs. [15–18]).

However, these approximate derivations are intrinsically isotropic, in the sense that they cannot account for the angular variations of the correction between the measurements, on the one hand, and the probed dynamics, on the other hand, in investigations of orientation-resolved photoemission [16,17,19–22]. The probe-induced anisotropy is particularly striking in the seminal work published in Ref. [23], where RABBIT measurements of atomic photoemission delays in He display significant angular variations, while the probed Wigner delay associated with single-photon ionization in this case is isotropic.

From a fundamental perspective, this asymmetry is related to the dipole selection rules in one- and two-photon processes and to the so-called Fano propensity rules [24] applied to two-photon ionization [25,26]. These rules formalize an imbalance in the angular momentum distribution in the two arms of the RABBIT interferometer, resulting in an angular redistribution of the modulus and phase of the photoemission probability amplitudes. By using standard asymptotic expansion of the continuum wave functions, the original analytical derivations of the probe influence in RABBIT measurements of photoemission delays [7,9,12] fail to account for these two-photon Fano propensity rules.

In this article we derive a semianalytic alternative representation of the continuum wave functions which is sufficient to recover, at least qualitatively, the asymmetric influence of the probe in RABBIT measurements. We use an expansion of the continuum wave functions up to the first order in r^{-1}, using the Wentzel-Kramers-Brillouin (WKB) approximation [27]. In this framework, our semianalytical expressions appear explicitly as an improvement over the standard derivations and are sufficient to retrieve the Fano propensity rules. Moreover, the WKB approach, by its semiclassical nature, is particularly suited to extract intuitive physical insight from the obtained analytical results. In Sec. II we review the formalism used in RABBIT, in terms of phases, delays, transitions amplitudes, and continuum wave functions. In Sec. III, focused on the question of anisotropy, we present our approach and demonstrate its ability to reproduce the two-photon Fano propensity rules. In Sec. IV we illustrate the consistency of our work with respect to a selection of previously published studies. We furthermore exploit its potential to provide finer insight to state-of-the art modeling and interpretation of time-resolved photoemission measurements. We provide a summary and conclusions in Sec. V.

*Contact author: richard.taieb@sorbonne-universite.fr

 ©2024 American Physical Society

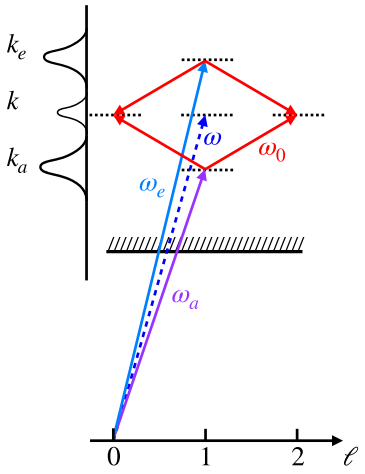

FIG. 1. Principle of the RABBIT scheme with angular momentum resolution. The two-photon transitions are indicated by solid arrows. The dashed-line arrow shows the virtual one-photon transition meant to be probed with the RABBIT scheme according to Refs. [7,9]. See the text for details.

II. MEASURING PHOTOEMISSION DELAYS WITH RABBIT

A. Measurable atomic delay

In this paper we focus on the temporal information encoded by a given sideband in a RABBIT scheme, as sketched in Fig. 1 and summarized hereafter. We consider the photoemission of an atom by a pair of consecutive XUV odd harmonics (with frequencies ω_a and ω_e) of an IR field, in the presence of the fundamental field (typically 800 nm wavelength, which corresponds to a photon energy $\omega_0 = 1.55$ eV). The obtained photoelectron spectrum contains two main peaks separated by $2\omega_0$, corresponding to the absorption of each harmonic, and an additional sideband peak in between, resulting from two-photon transitions involving the harmonics and the IR field. The energy relationship between the considered harmonics and the fundamental IR field is such that two quantum paths lead to the sideband formation: absorption of the lowest harmonic and absorption of an IR photon (labeled a in Fig. 1 and in the following) and absorption of the highest harmonic and emission of an IR photon (e).

When considering orientation-resolved measurements, the photoelectron momentum distribution associated with the sideband is hence expressed as the coherent sum

$$\mathcal{I}(\mathbf{k};\tau_{\mathrm{IR}}) \propto \left| M_a(\mathbf{k}) F_a \mathrm{e}^{-\mathrm{i}\varphi_a - \mathrm{i}\omega_0\tau_{\mathrm{IR}}} + M_e(\mathbf{k}) F_e \mathrm{e}^{-\mathrm{i}\varphi_e + \mathrm{i}\omega_0\tau_{\mathrm{IR}}} \right|^2. \tag{1}$$

In this expression F_a and F_e are the field strengths of the two harmonics, labeled according to the path to which they contribute, φ_a and φ_e are the associated phases, and $\omega_0\tau_{\mathrm{IR}}$ corresponds to the phase of the IR field, here written as a function of the experimentally tunable IR delay τ_{IR} with respect to the XUV. The factors $M_a(\mathbf{k})$ and $M_e(\mathbf{k})$ are the two-photon transition matrix elements associated with each path [28,29], where $\mathbf{k}$ is the photoelectron's asymptotic momentum vector. Investigating the dynamics of photoemission in RABBIT experiments consists in interpreting the so-called atomic phase corresponding to

$$\Delta\phi_A(\mathbf{k}) = \arg M_a(\mathbf{k}) - \arg M_e(\mathbf{k}). \tag{2}$$

This phase is accessible through a series of $\mathcal{I}(\mathbf{k};\tau_{\mathrm{IR}})$ measurements scanning τ_{IR} and calibrated with respect to the harmonic phases [7]. Various time-domain interpretations of the atomic phase have been proposed over the years (see, e.g., Ref. [30] and references therein). Here we consider the approach first introduced in [7] which consists in defining an atomic delay

$$\tau_A(\mathbf{k}) = -\frac{\Delta\phi_A(\mathbf{k})}{2\omega_0}, \tag{3a}$$

and relating it to the Wigner delay [31]

$$\tau_W(\mathbf{k}) = \frac{1}{k}\frac{\partial\eta(\mathbf{k})}{\partial k}, \tag{3b}$$

associated with a virtual one-photon process leading to the sideband energy $E = k^2/2$ (see the dashed arrow in Fig. 1). In the expression (4), $\eta(\mathbf{k})$ is the usual scattering phase shift of the photoelectron [32] which result only from the system- and channel-specific short-range contributions. Any attempt to relate $\tau_A(\mathbf{k})$ to $\tau_W(\mathbf{k})$ implies that the continuum is smooth enough for $\eta(\mathbf{k})$ to vary almost linearly within the $2\omega_0$-wide spectral range separating the two consecutive harmonic peaks. Thus, $\tau_A(\mathbf{k})$ can be seen as a finite-difference approximation of $\tau_W(\mathbf{k})$ [7], up to a correction

$$\tau_{\mathrm{cc}}(\mathbf{k}) = \tau_A(\mathbf{k}) - \tau_W(\mathbf{k}). \tag{3c}$$

In this context, RABBIT thus appears as an XUV-pump IR-probe scheme to access the dynamics of one-photon ionization in terms of Wigner delays. However, its full exploitation requires the knowledge of the correction term $\tau_{\mathrm{cc}}(\mathbf{k})$.

Insight into this term is obtained by expanding the transition amplitudes $M_a(\mathbf{k})$ and $M_e(\mathbf{k})$ according to the second-order perturbation theory, with an *ad hoc* representation of the continuum wave functions. This is addressed in the following, with the objective of accounting for the anisotropy of $\tau_{\mathrm{cc}}(\mathbf{k})$, i.e., the anisotropy induced by the probe stage in the RABBIT scheme, a consequence of the two-photon transition selection rules observed both in numerical simulations [16] and in experiments [23].

B. Second-order perturbation theory

In order to focus on the anisotropy specifically brought by the two-photon processes rather than by the initial state or by the ionic potential (see [17,33] and references therein), we consider the case of a spherically symmetric $\ell = 0$ initial state and linearly polarized collinear fields. By choosing the polarization direction as the quantization axis, the orbital magnetic quantum number $m = 0$ is conserved during the processes. More importantly, a single angular momentum channel ($\ell = 1$) is open in one-photon ionization, i.e., $\eta(\mathbf{k}) = \eta_1(k)$ for all momentum directions $\hat{k}$, k denoting the momentum magnitude. In contrast, two channels ($L = 0, 2$) are open in a two-photon process (see Fig. 1). In other words, the dynamics of the probed process is isotropic, while the probe process, and hence $\tau_{\mathrm{cc}}(\mathbf{k})$, is anisotropic.

For each path ($\alpha = a, e$), the two-photon transition matrix element reads [9]

$$M_\alpha(\mathbf{k}) = \frac{(8\pi)^{5/2}}{6\mathrm{i}} \sum_{L=0,2} C_{L0} Y_{L0}(\hat{k}) \mathrm{e}^{\mathrm{i}\eta_L(k)} T_L^\alpha(k), \tag{4}$$

where $C_{00} = 1/2$ and $C_{20} = -1/\sqrt{5}$ are the appropriate Clebsch-Gordan coefficients, Y_{L0} are the normalized spherical harmonics, and η_L are the scattering phases of the open channels $L = 0, 2$. We emphasize that the phase of interest is ultimately $\eta_1(k)$, which does not appear explicitly in Eq. (4) but emerges from the radial integrals $T_L^\alpha(k)$. The latter can be expressed as[1] [29]

$$T_L^\alpha(k) = \langle R_{kL} | \, r \, | \rho_{k_\alpha 1} \rangle \,, \tag{5}$$

where $R_{kL}(r)$ is the radial component of the final state's (reduced) wave function in channel L and $\rho_{k_\alpha 1}(r)$ the radial part of the so-called first-order perturbed wave function defined as

$$\rho_{k_\alpha 1}(r) = \lim_{\epsilon \to 0^+} \sum_\nu R_{\nu 1}(r) \frac{\langle R_{\nu 1} | \, r \, | R_0 \rangle}{E_0 + \omega_\alpha - E_\nu + \mathrm{i}\epsilon}. \tag{6}$$

All through the paper, we assume $E_0 + \omega_\alpha > 0$ (with E_0 the initial energy and ω_α the XUV photon energy in the considered path) such that $\rho_{k_\alpha 1}$ behaves as a continuum wave function [34] with asymptotic momentum $k_\alpha = \sqrt{2(E_0 + \omega_\alpha)}$. With this notation, the time delay of the probed one-photon process [Eq. (3b)] can be approximated as the finite difference

$$\tau_W(\mathbf{k}) = \frac{\eta_1(k_e) - \eta_1(k_a)}{2\omega_0}. \tag{7}$$

In Eq. (6), $R_0(r)$ is the radial part of the initial state and the sum and integral span the $\ell = 1$ manifold of the complete atomic spectrum, each of its states being associated with the radial wave function $R_{\nu 1}(r)$ and energy E_ν. Note that, following the reasoning of Ref. [7], we have discarded in Eq. (6) the term resulting from the paths where the infrared photon is absorbed first, which is negligible compared with the one considered here.

According to Eq. (6), the dominant contribution to $\rho_{k_\alpha 1}(r)$ in each path is proportional to the resonant $R_{k_\alpha 1}(r)$, i.e., to the final wave function reached by the XUV alone in the probed process. This underlines the possibility to isolate $\eta_1(k_\alpha)$ in the phase of $M_\alpha(k)$.

In Ref. [7], standard asymptotic expansions of $R_{kL}(r)$ and $\rho_{k_\alpha 1}(r)$, i.e., up to zeroth order in r^{-1}, are used. This approximation somehow formalizes a commonly accepted hypothesis, according to which the IR transition in the RABBIT scheme takes place significantly after the XUV absorption, i.e., when the photoelectron is beyond the L-dependent short-range influence of ionic potential. Consequently, T_L^α is found independently of L, which eventually leads to an isotropic expression of τ_A, and therefore of τ_{cc}, as summarized in the Appendix.

In the next section we go beyond this approximation and present a semiclassical treatment of the two-photon transition amplitudes that provides a properly anisotropic [23,25,26] semianalytic derivation for τ_{cc}.

[1] All through the paper, the bra-ket notation designates the scalar product with respect to the radial coordinate r.

III. ACCOUNTING FOR ANISOTROPY

In order to let the scattering phase difference $\eta_1(k_e) - \eta_1(k_a)$ emerge from the RABBIT phase, we explicitly express the total phase of the continuum radial wave functions $\rho_{k_\alpha,1}(r)$ and $R_{kL}(r)$ in the generic form

$$S_{\kappa\ell}(r) = \underbrace{\kappa r + \frac{Z}{\kappa} \ln(2\kappa r) - \frac{\ell\pi}{2} + \eta_\ell(\kappa)}_{\equiv S^\infty_{\kappa\ell}(r)} + \Delta S_{\kappa\ell}(r). \tag{8}$$

Here κ is the asymptotic momentum norm, ℓ the angular momentum, and Z the charge of the photoelectron's parent ion. The first terms encompassed in $S^\infty_{\kappa\ell}(r)$, including $\eta_\ell(\kappa)$, correspond to the universal asymptotic phase of an ionic radial continuum wave function. Only this expression was considered in the seminal works on RABBIT measurements of photoemission delays [7,9] that led to an isotropic τ_{cc}. Here we explicitly add a term $\Delta S_{\kappa\ell}(r)$ to be determined, expected to include short-range effects and to account for the anisotropy of τ_{cc}. This term vanishes at large r such that

$$S_{\kappa\ell}(r) \underset{r\to\infty}{\sim} S^\infty_{\kappa\ell}(r). \tag{9}$$

A. WKB continuum wave functions

To proceed, we choose the WKB formalism [27] and furthermore restrict $\Delta S_{\kappa\ell}(r)$ to the first nonvanishing term in its expansion in powers of r^{-1}. The WKB approach provides both intuitive arguments in terms of classical mechanics and satisfactory quantitative results in related contexts (see, e.g., Ref. [35] and references therein). It was notably used in [9] to the order of r^{-1}, but to obtain a correction of the wave functions' modulus only. Within the WKB approach, the final continuum and intermediate first-order perturbed wave function are approximated as

$$R_{kL}(r) \simeq \frac{\sin[S_{kL}(r)]}{[k^2 - 2V_L(r)]^{1/4}}, \tag{10a}$$

and

$$\rho_{k_\alpha 1}(r) \simeq \frac{\exp\left[\mathrm{i}S_{k_\alpha 1}(r)\right]}{\left[k_\alpha^2 - 2V_1(r)\right]^{1/4}}, \tag{10b}$$

respectively, where $V_\ell(r)$ is the channel-dependent effective potential including the centrifugal term. In this framework, the phase $S_{\kappa\ell}(r)$ is approximated as the action (also known as the Hamilton characteristic function [36])

$$S_{\kappa\ell}(r) \simeq S_{\kappa\ell}(r_0) + \int_{r_0}^{r} \sqrt{\kappa^2 - 2V_\ell(r')}\, dr', \tag{10c}$$

where the value $S_{\kappa\ell}(r_0)$ at the arbitrary radius r_0 is enforced to fulfill the asymptotic boundary conditions given in Eq. (9).

In order to reveal the signatures of the ℓ-dependent centrifugal term in the two-photon matrix elements, we explicitly express the effective potential experienced by the photoelectron with momentum ℓ as

$$V_\ell(r) = -\frac{Z}{r} + \frac{\ell(\ell+1)}{2r^2} + O(r^{-3}). \tag{11}$$

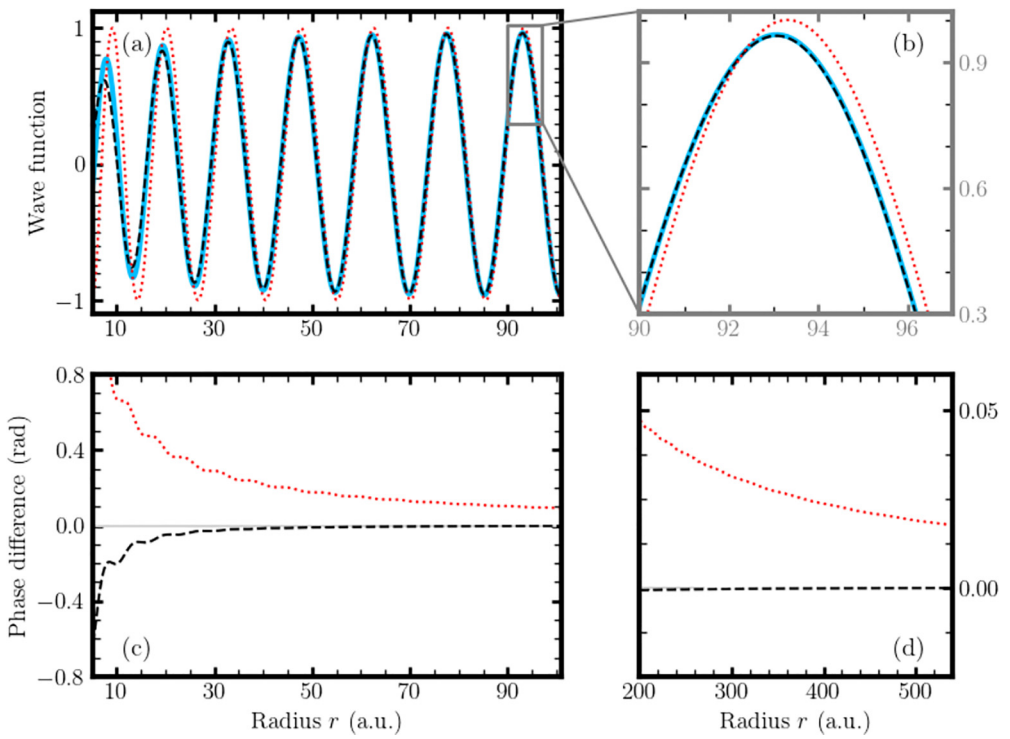

FIG. 2. Plot of the $L = 0$ continuum state of the hydrogen atom at $k = 0.37$ a.u. (a) and (b) Radial wave function obtained as the exact solution of the time-independent Schrödinger equation (blue solid line), as the approximation given by Eq. (10a) including $\beta_{\kappa\ell}$ (black dashed line), and as the standard approximation [7,9] discarding $\beta_{\kappa\ell}$ (red dotted line). (c) and (d) Phase difference between each of the two approximate wave functions [same color code as in (a) and (b)] and the exact one. The left and right columns highlight two different radius ranges.

With the WKB expressions (10) and neglecting the $O(r^{-3})$ terms in Eq. (11), we find that the leading term when expanding the WKB action $S_{\kappa\ell}(r)$ in powers of r^{-1} is the first-order term, i.e.,

$$\Delta S_{\kappa\ell}(r) = \frac{\mathrm{Re}\beta_{\kappa\ell}}{r} + O(r^{-2}), \tag{12}$$

with the complex-valued ℓ-dependent coefficient

$$\beta_{\kappa\ell} = \frac{1}{2\kappa^3}\big[\ell(\ell+1)\kappa^2 + Z^2 + \mathrm{i}Z\kappa\big], \tag{13}$$

the imaginary part of which comes from the expansion of the denominator in Eq. (10). The first term is related to the short-range centrifugal potential $\ell(\ell+1)/2r^2$ and the last two terms are imprints of the Coulomb tail $-Z/r$.

Eventually, we obtain WKB approximations of the radial continuum wave functions, up to the first order in r^{-1}, behaving asymptotically as

$$R_{kL}(r) = \frac{1}{\sqrt{k}} \mathrm{e}^{-\mathrm{Im}\beta_{kL}/r} \sin\big[S^{\infty}_{kL}(r) + \mathrm{Re}\beta_{kL}/r\big] + O(r^{-2}), \tag{14a}$$

$$\rho_{k_\alpha 1}(r) = \frac{1}{\sqrt{k_\alpha}} \mathrm{e}^{-\mathrm{Im}\beta_{k_\alpha 1}/r} \mathrm{e}^{\mathrm{i}[S^{\infty}_{k_\alpha 1}(r) + \mathrm{Re}\beta_{k_\alpha 1}/r]} + O(r^{-2}). \tag{14b}$$

Note that, at zeroth order in r^{-1}, the expressions (10) lead to the standard wave functions used in Ref. [7].

To highlight the importance of the $\Delta S_{\kappa\ell}(r)$ corrections at short and long distances, we assess our approach with the hydrogen atom, for which exact results are available [27] [in particular, $\eta_\ell(k) = \Gamma(\ell + 1 + \mathrm{i}Z/k)$]. As an illustration, we show in Figs. 2(a) and 2(b) the $L = 0$ and $k = 0.37$ a.u. radial wave functions. The numerically exact solution of the time-independent Schrödinger equation is shown as a blue solid line, the WKB approximation given in Eq. (10a) as a black dashed line, and the lowest-order equivalent, corresponding to $\beta_{\kappa\ell} = 0$, as a red dotted line. We see in Fig. 2(b) that both approximate wave functions converge asymptotically to the exact solution. However, our WKB continuum wave function converges much faster to the exact solution due to its r^{-1} corrections, as seen in the shorter range displayed in Fig. 2(a). Here we see that the imaginary part of $\beta_{\kappa\ell}$ modulates the amplitude of the wave function in the short range, which qualitatively reproduce the behavior of the exact wave function [9]. That modulation is formally absent in the zeroth-order wave function.

For more comprehensive insight, we plot in Figs. 2(c) and 2(d) the phase difference between each approximate wave function and the exact one (same color code). We see in Fig. 2(c) that including the correction allows a much faster convergence of the phase, within a few tens of a.u. At $r = 40$ a.u, the error is -0.015 rad only when $\beta_{\kappa\ell}$ is properly included, while it is an order of magnitude larger (0.218 rad) when enforcing $\beta_{\kappa\ell} = 0$. Moreover, Fig. 2(d) underlines the improvement of our approach with respect to the zeroth-order approximation even at larger distances, where the latter converges slowly (in r^{-1}) while the former accurately matches the exact phase. This is particularly important in the context of the present study because the integrals involved in the matrix element computation are mainly driven by the long-range

oscillations of $\rho_{k_\alpha 1}(r) \propto R_{k_\alpha 1}(r)$ and of $R_{kL}(r)$ (discussed below).

More generally, the phases $S_{\kappa\ell}$ play a central role in interferometric schemes such as the RABBIT. In the next section, we show how the corrections $\Delta S_{\kappa\ell}$ impact the angular dependence of the measurable atomic delays.

B. Anisotropy of the atomic delay

We now use our approximate representation of the continuum wave functions to evaluate the two-photon matrix elements involved in the RABBIT process, their phases, and the corresponding atomic delay. By substituting Eqs. (10) into (5) and neglecting the phase term proportional to $S_{kL}+S_{k_\alpha 1}$ following Ref. [7] (rotating-wave approximation), we obtain

$$T_L^\alpha(k) \simeq \int_0^\infty dr \frac{r \exp\left\{-\mathrm{i}\left[S_{kL}(r) - S_{k_\alpha 1}(r)\right]\right\}}{\left[k^2 - 2V_L(r)\right]^{1/4}\left[k_\alpha^2 - 2V_1(r)\right]^{1/4}}. \tag{15}$$

By approximating $S_{\kappa\ell}(r)$ by $S_{\kappa\ell}^\infty(r)+\mathrm{Re}\beta_{\kappa\ell}/r$ and $[\kappa^2-2V_\ell(r)]^{-1/4}$ by $\exp(-\mathrm{Im}\beta_{\kappa\ell}/r)/\sqrt{\kappa}$ consistently with Eqs. (14), we obtain an analytic expression for the radial two-photon transition matrix elements

$$T_L^\alpha(k) \simeq \frac{-\mathrm{i}^L}{\sqrt{k k_\alpha}} \mathrm{e}^{\mathrm{i}[\eta_1(k_\alpha)-\eta_L(k)]} \times \frac{(2k_\alpha)^{\mathrm{i}Z/k_\alpha}}{(2k)^{\mathrm{i}Z/k}} \mathbb{M}(\underbrace{Z/k_\alpha - Z/k}_{\equiv s}, \underbrace{k_\alpha - k}_{\equiv \Delta k}, \underbrace{\beta_{k_\alpha 1} - \beta_{kL}^*}_{\equiv \Delta\beta_L}), \tag{16a}$$

with

$$\mathbb{M}(s, \Delta k, \Delta\beta_L) \equiv \frac{1}{2}\int_0^\infty r^{1+\mathrm{i}s} \exp\left(\mathrm{i}\Delta k r + \mathrm{i}\frac{\Delta\beta_L}{r}\right) dr = \left(\frac{\Delta\beta_L}{\Delta k}\right)^{1+\mathrm{i}s/2} K_{2+\mathrm{i}s}(-2\mathrm{i}\sqrt{\Delta\beta_L \Delta k}), \tag{16b}$$

where $K_\nu(z)$ is the modified Bessel function of the second kind. Note that, as mentioned earlier, in Ref. [9] the correction in r^{-1} has been considered only in the modulus of the continuum wave function, i.e., corresponding to taking the real part of $\beta_{\kappa\ell}$ to be zero.

The atomic phase $\tau_A(\mathbf{k})$ can then be evaluated by inserting the analytical expression (16a) in Eq. (4). The expression (16a) shows explicitly that $\eta_1(k_e)-\eta_1(k_a)$ emerges and $\eta_L(k)$ disappears when expressing $\Delta\phi_A(\mathbf{k})$ out of $T_L^\alpha(k)$, as in [7]. Here $\tau_A(\mathbf{k})$ and therefore $\tau_{cc}(\mathbf{k})$ are anisotropic due to the explicit L dependence of $\arg T_L^\alpha$. We now turn to the comparison of the results with *ab initio* numerical calculations.

Figure 3 shows the angular variations of the atomic delay $\Delta\tau_A(k,\theta) = \tau_A(k,\theta) - \tau_A(k,0)$ as a function of the emission angle θ with respect to the polarization axis, for a few values of the asymptotic final momentum k. The WKB results obtained from Eq. (16a) are shown with dashed lines and the ones obtained from numerically exact calculations with solid lines. All the curves follow a similar trend. First, $\Delta\tau_A$ remains constant, close to zero, for $0° < \theta \lesssim 60°$ at all k. Then a sudden jump takes place, spanning several hundred attoseconds over few 10°, before reaching a stable value for

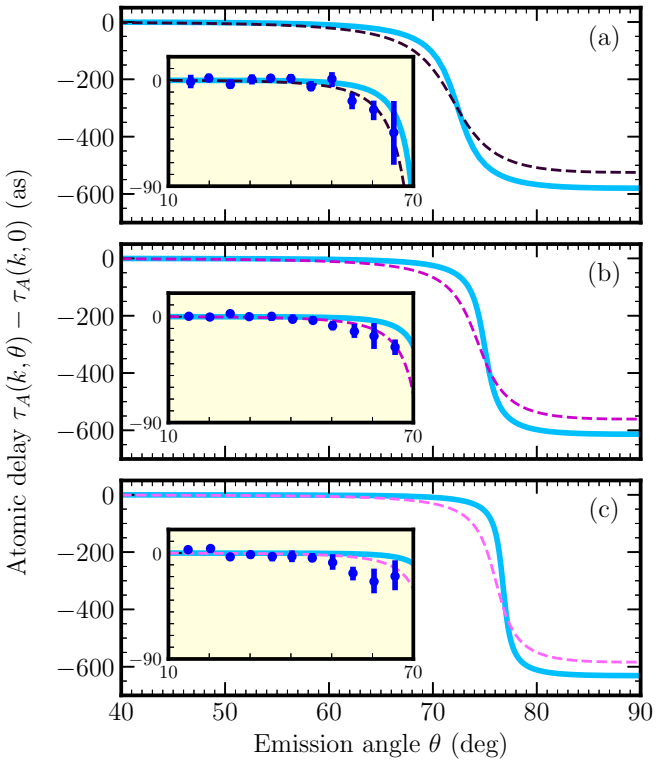

FIG. 3. Angular variations of the atomic delay $\tau_A(\theta) - \tau_A(0°)$ in photoemission from a neutral atom. Data were obtained from the numerically exact simulations on the H atom [37] (solid lines), using the analytical WKB derivation with $Z = 1$ from Eqs. (16) (dashed lines), and experimentally on He reproduced from [23] (blue dots with error bars). Each panel is associated with a given asymptotic final momentum (see Fig. 1): (a) $k = 0.61$ a.u., (b) $k = 0.77$ a.u., and (c) $k = 0.91$ a.u.

larger θ values. In addition, we make the two following observations when k increases: (i) The critical angle θ_c around which the jump occurs increases and (ii) the jump gets sharper and its magnitude converges towards approximately $\pi/2\omega_0$. The latter is the signature of a change of sign in the dominant contribution $M_a(\mathbf{k})$ to the overall amplitude [25]. In the context of RABBIT measurements of one-photon ionization delays, this remarkable ω_0-dependent feature underlines the probe origin of the measured τ_A anisotropy [23].

These k- and θ-dependent trends, observed in the exact simulations (thick blue lines), are qualitatively reproduced by our analytical WKB results (dashed lines). Quantitatively, we note that θ_c are overestimated in the analytical predictions by about 5° compared to the exact solutions and the $\Delta\tau_A$ jump is less pronounced than in the exact simulations by about 50 as. These small differences can be related to the estimation of the WKB wave functions near the origin [see Fig. 2(a)]. Nevertheless, these results show that the approximate WKB wave functions expanded to the first order in r^{-1} are sufficient to recover the trend of the experimental results reported in [23], displayed as symbols with error bars in the insets of Fig. 3.

Therefore, our results show that the angular dependence of τ_{cc} mainly comes from an r^{-1} contribution to the photoelectron phase. This term plays a significant role because it

persists at large distances. It is itself the signature of the short-range influence of the centrifugal barrier, which indicates that the IR pulse, in the RABBIT setup, probes the photoelectron already at short distances.

C. Fano's propensity rules

We now revisit the anisotropy of RABBIT measurements in terms of Fano's propensity rules [24,25], in the light of our WKB-based approach.

In order to obtain an expression of τ_{cc} bearing relevant physical insight, we proceed with our analytical developments in the so-called soft-photon limit [38], which is achieved for either large k or small ω_0. The soft-photon approximation has often proved efficient in this context (see, e.g., Refs. [9,16]). This corresponds to considering $\Delta k/k$ small in the computation of the matrix elements expressed according to Eqs. (16a) and (16b), leading to

$$\mathbb{M}(s,\Delta k,\Delta\beta_L)\approx\frac{\Gamma(2+is)}{2(-i\Delta k)^{2+is}}\exp\left(\frac{\Delta k\,\Delta\beta_L}{1+is}\right), \tag{17}$$

where we have used standard limits of Bessel functions [39]. One should note that the isotropic results of [7,9] can be retrieved by setting $\Delta\beta_L=0$ *a posteriori* in this last expression of the matrix element.

Next, by substituting Eq. (17) into Eq. (16a) and expanding in terms of ω_0/k^2 up to the first order, we obtain the expression for the radial transition matrix element in the soft-photon regime

$$T_L^\alpha(k)\approx\frac{i^L k}{2\omega_0^2}e^{i[\eta_1(k_\alpha)-\eta_L(k)]}\exp\left(\epsilon_\alpha\frac{\omega_0}{2k^2}[2-L(L+1)]\right)\times\exp\left\{i\epsilon_\alpha\frac{\omega_0 Z}{k^3}\left[1+\gamma+\ln\left(\frac{\omega_0}{2k^2}\right)\right]\right\}, \tag{18}$$

where $\epsilon_a=-1$, $\epsilon_e=+1$, and $\gamma\approx0.577$ is the Euler-Mascheroni constant. Remarkably, at this level of approximation $\arg T_L^\alpha(k)$ does not depend on the final electron momentum L other than through the final scattering phase $\eta_L(k)$ (and i^L), in contrast to its modulus

$$|T_L^\alpha(k)|=\frac{k}{2\omega_0^2}\exp\left(\frac{\epsilon_\alpha\omega_0}{2k^2}[2-L(L+1)]\right). \tag{19}$$

This expression allows retrieving, in the soft-photon limit, the Fano propensity rules [25] of two-photon processes. Indeed, it tells us that $|T_2^a|\geqslant|T_0^e|\geqslant|T_0^a|\geqslant|T_2^e|$, i.e., the most probable ionization path in the RABBIT scheme is the one involving the IR absorption ($\alpha=a$) with $L=2$ while the least probable path is the one involving the IR emission ($\alpha=e$) for $L=2$. These propensity rules appear to result from the L dependence of the real part of the lowest order in ω_0/k^2 of

$$\Delta\beta_L=\frac{2-L(L+1)}{2k}+i\frac{Z}{k^2}+O\left(\frac{\omega_0}{k^2}\right), \tag{20}$$

and therefore from the r^{-1} term [Eq. (12)] in the continuum wave function phase [Eq. (8)].

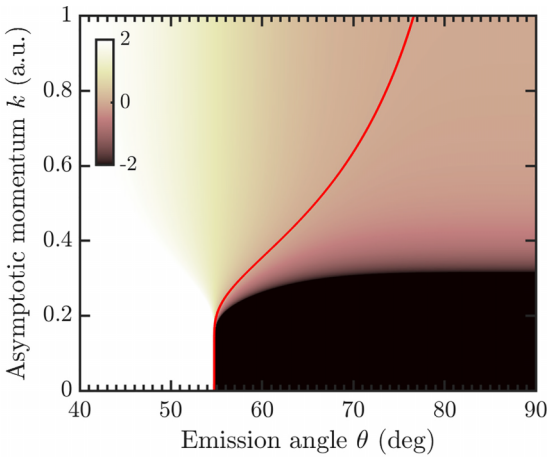

FIG. 4. Value of $f(\mathbf{k})$ given by Eq. (21b) as a function of the asymptotic momentum k and the emission angle θ. The red line indicates the critical angle θ_c around which the phase jump occurs, i.e., the solution of Eq. (22).

In terms of dynamics, the atomic delay τ_A in the soft-photon regime is obtained by substituting Eq. (18) into Eqs. (4) and (3c), leading to the expression

$$\lim_{\omega_0\to0}\tau_{cc}(\mathbf{k})=\frac{Z}{k^3}\left[1+\gamma+\ln\left(\frac{\omega_0}{2k^2}\right)\right]-\frac{1}{2\omega_0}\arg[f(\mathbf{k})], \tag{21a}$$

with the real-valued orientation-dependent function

$$f(\mathbf{k})=1-\frac{2C_{00}Y_{00}(\hat{k})C_{20}Y_{20}(\hat{k})}{[C_{00}Y_{00}(\hat{k})]^2+[C_{20}Y_{20}(\hat{k})]^2}\cosh\left(\frac{3\omega_0}{k^2}\right), \tag{21b}$$

for all Z. The angular jump observed in each frame of Fig. 3 is thus the signatures of a change of sign in f. This can occur only due to the cosh factor, whose presence is a direct manifestation of the Fano propensity rules. Indeed, this factor reduces to 1 if one sets $|T_2^a|=|T_0^a|$ and $|T_0^e|=|T_2^e|$, which is based on the original derivations of Refs. [7,9] (see the Appendix).

The characteristics of this Z- and k-dependent phase jump were modeled in Ref. [22] through a general formula parametrized with the interfering transition amplitudes. In particular, the angle θ_c around which the jump is centered increases for increasing ω_0/k^2. This is consistent with the general trend illustrated in Fig. 3 and noted above. Within our approach this angle is the solution of $f(\mathbf{k})=0$, which translates into a very simple formula

$$\cos^2(\theta_c)=\tfrac{1}{3}\left(1-e^{-3\omega_0/k^2}\right). \tag{22}$$

It is indicated by the red line in the (k,θ) map of Fig. 4.

Note that higher orders in the soft-photon expansions would be required to investigate the ω_0 dependence of $\tau_{cc}(k,180^\circ)-\tau_{cc}(k,0^\circ)$ revealed numerically on one-dimensional asymmetric model systems in [17].

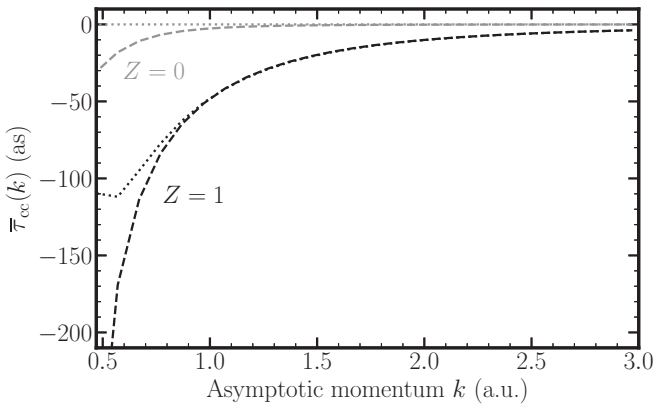

FIG. 5. Continuum-continuum time delays $\overline{\tau}_{cc}(k)$ from the integrated RABBIT scheme as a function of the asymptotic momentum k. The gray and black lines are for $Z = 0$ and $Z = 1$, respectively. The dashed lines show the data obtained with the radial two-photon transition matrix element (16a). The dotted lines correspond to the soft-photon approximation given by Eq. (25).

IV. LINKS WITH AVAILABLE DERIVATIONS AND INTERPRETATIONS

Here we highlight additional links between our semianalytical approach and existing derivations and interpretations and exploit the advantages of the WKB approach to gain further physical insights. We resort to the soft-photon approximation invoked in Sec. III C when it is helpful.

A. Orientation-averaged RABBIT

In the original RABBIT scheme [4], the atomic phase $\overline{\Delta\phi}_A(k)$ is extracted from the orientation-averaged photoelectron spectra

$$\overline{\mathcal{I}}(k;\tau_{IR}) = \int \mathcal{I}(\mathbf{k};\tau_{IR})d\hat{k}. \tag{23}$$

The atomic delay obtained in this context is then given by

$$\overline{\tau}_A(k) = -\frac{1}{2\omega_0}\arg\left(\sum_{L=0,2}|C_{L0}|^2 T_L^a(k)T_L^e(k)^*\right). \tag{24}$$

In the same way as for the angularly resolved case, the angle-integrated continuum-continuum correction is defined as $\overline{\tau}_{cc}(k) = \overline{\tau}_A(k) - \overline{\tau}_W(k)$. Note that, if the probed one-photon transition ends up in a single angular momentum channel as considered throughout the paper, $\overline{\tau}_W(k) = \tau_W(\mathbf{k})$ in all momentum directions. Otherwise, if it ends up in a combination of angular momenta, i.e., starting from an $\ell \neq 0$ initial state, then the Wigner delay $\overline{\tau}_W(k)$ associated with an orientation-averaged measurement is ill-defined. In the soft-photon limit, we find that

$$\lim_{\omega_0\to 0}\overline{\tau}_{cc}(k) = \frac{Z}{k^3}\left[1+\gamma+\ln\left(\frac{\omega_0}{2k^2}\right)\right]. \tag{25}$$

This result corresponds to the isotropic contribution of the angularly resolved case given by Eq. (21). We have verified that Eq. (25) can be derived by taking the soft-photon limit of Eq. (100) in Ref. [9]. Figure 5 compares $\overline{\tau}_{cc}$ obtained from the radial two-photon transition matrix element [Eq. (16a)] (dashed lines) and within the soft-photon approximation [Eq. (25)] (dotted lines), for $Z = 1$ (black lines) as well as for $Z = 0$ (gray lines). We observe that for all $k \gtrsim 1$, the soft-photon approximation provides a very good estimate of the actual $\overline{\tau}_{cc}$. Note that, when neglecting the long-range term (in r^{-1}) in the wave function, the resulting expression significantly differs from Eq. (25) (see the Appendix).

The expression (25) is reminiscent of the one obtained from empirical classical arguments in Ref. [12], i.e.,

$$\overline{\tau}_{cc}(k) \approx \frac{Z}{k^3}\left[2+\ln\left(\frac{\omega_0}{\pi k^2}\right)\right]. \tag{26}$$

It was shown to reproduce well *ab initio* calculations in the soft-photon regime [16,17]. The absolute difference between the expressions from Eqs. (21) and (26) is $[\gamma - 1 + \ln(\pi/2)]Z/k^3 \simeq 0.03\times Z/k^3$, which indeed vanishes far from threshold.

B. Atomic delays in photodetachment processes

We now consider photodetachment processes from closed-shell negative ions, as investigated numerically in Refs. [40,41] from the delay perspective. In this case, the effective potential is given by Eq. (11) with $Z = 0$. It is short range and asymptotically dominated by the centrifugal barrier. As a consequence, the radial dependence of the asymptotic phase $S_{\kappa\ell}^{\infty}(r)$ of the continuum wave function in Eq. (8) is essentially κr, which corresponds to a free particle. Regarding the coefficient of the correcting term $\Delta S_{\kappa\ell}(r)$ at order r^{-1} [Eq. (12)], it becomes $\beta_{\kappa\ell} = \ell(\ell+1)/2\kappa$. Therefore, even in the presence of short-range interactions only, the phase maintains a long-range behavior.

In order to analyze the photodetachment dynamics, we start by comparing the continuum-continuum time delays from the integrated RABBIT scheme shown in Fig. 5 and discussed in the preceding section. For increasing k, $\overline{\tau}_{cc}(k)$ goes faster to zero for $Z = 0$ than for $Z = 1$, and the photodetachment time-delay practically vanishes beyond $k \approx 1$, in agreement with Ref. [40]. This is consistent with the hypothesis according to which, in a RABBIT experiment, the interaction with the IR photon takes place outside the effective range of the atomic potential, including the centrifugal term, leading to $\overline{\tau}_A(k) \approx \overline{\tau}_W(k)$. Note, however, that numerical simulations evidence near-threshold system-specific deviations from this universal behavior, as shown in Fig. 7 of Ref. [40]. This can be accounted for in our approach by correcting the expression of $\beta_{\kappa\ell}$ [Eq. (13)] with any contribution of the r^{-2} term in the polarization potential of the considered anion. Meanwhile, when looking at the angularly resolved data (see Fig. 6) we observe an angular dependence which is as pronounced as in the photoionization case $Z = 1$ (see Fig. 3). Indeed, as explained in Sec. III C, the main features of this angular dependence are related to the universal centrifugal barrier. Therefore, the IR transitions occur under the influence of the latter also in the photodetachment case, even though it does not manifest in the angularly integrated data.

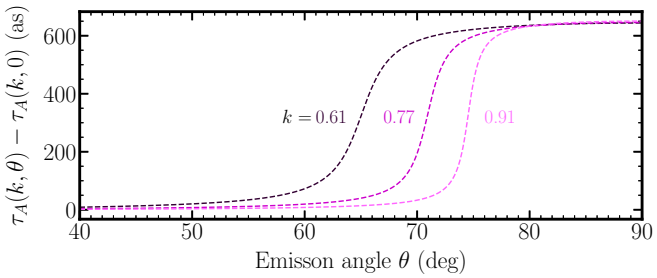

FIG. 6. Angular variations of the atomic delay $\tau_A(k,\theta) - \tau_A(k,0^\circ) = \tau_{cc}(k,\theta) - \tau_{cc}(k,0^\circ)$ in a photodetachment process. Data were obtained using Eqs. (16) with $Z = 0$. The dark violet, medium purple, and light pink lines correspond to values of the final asymptotic momentum $k = 0.61$, 0.77, and 0.91 a.u., respectively.

C. Classical perspective on the Fano propensity rules

In this section we exploit the WKB formalism to pinpoint the dominant paths in the two-photon process and highlight the classical mechanisms behind Fano's propensity rules discussed in Sec. III C. We start with the WKB expression of $T_L^\alpha(k)$ given by Eq. (15) and note that it is reminiscent of the single-photon form discussed by Fano in Ref. [24]. Its integrand contains an oscillating complex term $\exp[i(S_{kL} - S_{k_\alpha 1})]$. Following Fano's arguments and inspired by the saddle-point approximation, the modulus of this integral is larger if there exists a real-valued position for which the derivative of the phase vanishes. More explicitly, this corresponds to the conditions

$$p_{kL} = p_{k_\alpha 1}, \tag{27}$$

where

$$p_{\kappa\ell}(r) \equiv \frac{\partial S_{\kappa\ell}(r)}{\partial r} = \sqrt{\kappa^2 - 2V_\ell(r)}, \tag{28}$$

is the local momentum obtained from the Hamilton characteristic function $S_{\kappa\ell}$ given in Eq. (10c) [36].

We now turn to the identification of the paths, among those involved in a RABBIT scheme, fulfilling Eq. (27) or not. As an illustration, we consider the case of $Z = 1$ and $k = 0.37$. Figure 7 shows trajectories $(r, p_{\kappa\ell})$ in a phase-space-like representation, for the different κ and ℓ associated with the intermediate and final states. The absorption and emission paths are shown in Figs. 7(a) and 7(b), respectively. In each frame, the $(r, p_{k_\alpha 1})$ and (r, p_{kL}) trajectories are represented by thick and thin lines, respectively. The existence of a real-valued saddle point fulfilling (27) is therefore revealed by an intersection between thick and thin lines. Note that the trajectories can possibly intersect because they are associated with different effective potentials V_ℓ.

The trajectories possessing such a point are highlighted by solid lines, while the others are shown with dashed lines. In Fig. 7(a) ($\alpha = a$), only the trajectory (r, p_{k2}) intersects with $(r, p_{k_a 1})$, and therefore the dominant quantum path is the $L = 2$ channel. In Fig. 7(b) ($\alpha = e$), only the trajectory (r, p_{k0}) intersects with $(r, p_{k_e 1})$, and therefore the dominant quantum path is the $L = 0$ channel. Hence, this perspective expands the classical arguments implied by Fano's discussion of the propensity rules in Ref. [24] to the two-photon case [25].

V. CONCLUSION

To summarize, we have used the WKB formalism to obtain approximate atomic continuum wave functions that provide a qualitative account of Fano's propensity rules in two-photon ionization [24]. The latter are responsible for the probe-induced asymmetry in interferometric RABBIT measurements of the Wigner delay characterizing the one-photon ionization dynamics [16,23,25].

Our derivations provide analytical expressions of the radial two-photon transition matrix elements [Eq. (18)] and of the so-called atomic delay τ_A [Eqs. (21)], in the soft-photon regime. It notably accounts for the angular jump of nearly π rad in the argument of the RABBIT transition matrix element, due to Fano's propensity rules. This jump leads to a pronounced anisotropy of the atomic time delay measurements, i.e., an angular jump of approximately $\pi/2\omega_0$ in terms of delay. We have shown that this probe-induced asymmetry of τ_A can be traced back to a universal long-range behavior, in r^{-1}, of the continuum wave function, which is inherited from the long-range Coulomb tail of the ionic potential as well as from the ℓ-dependent short-range centrifugal potential.

We then further investigated how our approach relates to other previously published results. When considering orientation-averaged RABBIT measurements, we have obtained an analytical expression of the atomic time delay $\overline{\tau}_A$ [Eq. (25)] that is remarkably close to the one obtained semiempirically in Ref. [12] and that has proved efficient

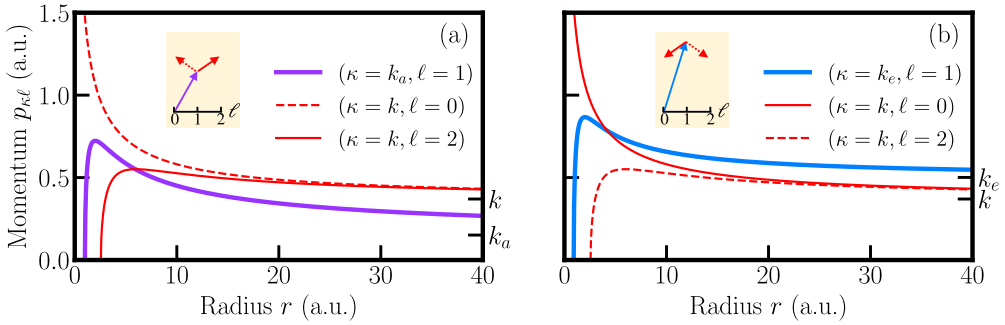

FIG. 7. Local momentum $p_{k\ell}$ [Eq. (28)] as a function of the radius in (a) intermediate states ($\ell = 1$) and (b) final states ($\ell = 0, 2$) involved in the two arms of the interferometric 800-nm RABBIT scheme. The considered asymptotic final momentum is $k = 0.37$ such that the asymptotic intermediate momenta are $k_a = 0.15$ a.u. and $k_e = 0.50$ a.u.

in comparisons with numerical simulations [16,17]. We have also investigated the anisotropy of the atomic delay in photodetachment processes, previously studied numerically in Ref. [40] from the orientation-averaged perspective. Our results show that the anisotropy is as pronounced as in the photoionization case, since it appears as an imprint of the universal centrifugal potential on the scattering phase.

Eventually, we exploited the classical insight offered by the WKB approximation to highlight an intuitive interpretation of Fano's propensity rules in terms of momentum conservation [24], by evaluating the transition matrix elements with the saddle-point approximation. The simplicity of the analytical formulas obtained here offers a promising framework for the investigation of photoemission time delays in atomic systems from initial states carrying a nonzero orbital quantum number [19,42] and more generally in systems with additional degrees of freedom [15,43–45] and beyond the RABBIT regime [46].

ACKNOWLEDGMENTS

This research received financial support from the French 866 National Research Agency through Grants No. ANR-20-CE30-0007-868-DECAP and No. ANR-21-CE30-0036-03-ATTOCOM.

APPENDIX: ZEROTH-ORDER DERIVATIONS AND PREDICTIONS

In this Appendix we recall the theory of Refs. [7,9] to approximate the radial two-photon transition matrix elements in Eq. (5). We then show the predictions it leads to in terms of photoemission time delays, regardless of the WKB approximations used in the present paper.

Using the paper's notation, the continuum wave functions in Eq. (5) are approximated by asymptotic Coulombic wave functions

$$R_{kL}(r) = \frac{1}{\sqrt{k}} \sin\left[S^{\infty}_{kL}(r)\right] + O(r^{-1}), \tag{A1a}$$

$$\rho_{k_\alpha 1}(r) = \frac{1}{\sqrt{k_\alpha}} e^{iS^{\infty}_{k_\alpha 1}(r)} + O(r^{-1}), \tag{A1b}$$

where the expression of $S^{\infty}_{\kappa\ell}(r)$ is defined in Eq. (8). Substituting Eqs. (A1) in Eq. (5) leads to radial two-photon transition matrix elements of the form

$$T^{\alpha}_{L}(k) \simeq \frac{-i^{L}}{\sqrt{kk_\alpha}} e^{i[\eta_1(k_\alpha)-\eta_L(k)]} \frac{(2k_\alpha)^{iZ/k_\alpha}}{(2k)^{iZ/k}} \frac{\Gamma(2+is)}{2(-i\Delta k)^{2+is}}. \tag{A2}$$

As a consequence, in this case, all radial two-photon matrix elements are related through

$$i^{L} T^{\alpha}_{L}(k) e^{i\eta_L(k)} = T^{\alpha}_{0}(k) e^{i\eta_0(k)}, \tag{A3}$$

for all L. The relation (A3) has drastic consequences in the angularly resolved atomic time delay and the one obtained from the integrated RABBIT measurements that are intrinsic to the approximation (A1) that we detail below. Substituting Eq. (A3) in Eq. (4), we obtain

$$M_\alpha(\mathbf{k}) = (8\pi)^{5/2} \frac{i e^{i\eta_0(k)} T^{\alpha}_{0}(k)}{6\sqrt{kk_\alpha}} \sum_{L=0,2} i^{L} C_{L0} Y_{L0}(\hat{k}). \tag{A4}$$

The atomic phase from Eq. (2) simplifies to

$$\Delta\phi_A(\mathbf{k}) = \arg\left[T^{a}_{0}(k)\right] - \arg\left[T^{e}_{0}(k)\right]. \tag{A5}$$

Therefore, it is independent of the asymptotic momentum angle $\hat{k}$, i.e., $\tau_W(\mathbf{k})$ and $\tau_{cc}(\mathbf{k})$ are isotropic.

We now turn to the atomic phase obtained from the angularly integrated RABBIT scheme whose expression is given in Eq. (24). Here again we use the relation (A3) and we obtain

$$\overline{\Delta\phi}_A(k) = \arg\left[T^{a}_{0}(k)\right] - \arg\left[T^{e}_{0}(k)\right]. \tag{A6}$$

Hence, $\Delta\phi_A(\mathbf{k}) = \overline{\Delta\phi}_A(k)$ and $\tau_{cc}(\mathbf{k}) = \overline{\tau}_{cc}(k)$. In the soft-photon limit discussed in Sec. III C, we find in this case

$$\lim_{\omega_0\to 0} \overline{\tau}_{cc}(k) = \frac{Z}{k^3}\left[\gamma + \ln\left(\frac{\omega_0}{2k^2}\right)\right], \tag{A7}$$

which differs significantly from the empirical formula given by Eq. (26) and the one derived in this article (25). Moreover, for the photodetachment described in Sec. IV B, i.e., for $Z = 0$, all terms on the right-hand side of Eq. (A2) become real except the ones coming from the scattering phase. Hence,

$$\overline{\Delta\phi}_A(k) = \eta_1(k_a) - \eta_1(k_e), \tag{A8}$$

which is the Wigner phase delay, and $\tau_{cc}(k) = 0$ for all asymptotic momenta. In contrast, it is nonvanishing in the numerical simulations [40] for intermediate k.

To conclude, features observed in the numerical simulations [16] and the experiments [23] are not present in the approximation used in [7,9] and summarized in this Appendix. The main issues are the following: The continuum-continuum time delay $\tau_{cc}(\mathbf{k})$ is isotropic (including for $Z = 0$), the soft-photon regime is not well reproduced, and $\tau_{cc}(\mathbf{k})$ vanishes for $Z = 0$, including near threshold. These features cannot be captured by the approximation (A1) because they result from the long-range behavior in r^{-1} of the continuum wave functions included in our approach, as demonstrated in the main text. Note that they are still not captured if the correction r^{-1} is included only in the amplitude of the continuum wave functions (and not in their phase) as in Ref. [9], except for the soft-photon regime as described below Eq. (25).

[1] P. Agostini and L. F. DiMauro, The physics of attosecond light pulses, Rep. Prog. Phys. **67**, 813 (2004).

[2] F. Krausz and M. Ivanov, Attosecond physics, Rev. Mod. Phys. **81**, 163 (2009).

[3] M. Hentschel, R. Kienberger, C. Spielmann, G. A. Reider, N. Milosevic, T. Brabec, P. Corkum, U. Heinzmann, M. Drescher, and F. Krausz, Attosecond metrology, Nature (London) **414**, 509 (2001).

[4] P. M. Paul, E. S. Toma, P. Breger, G. Mullot, F. Augé, P. Balcou, H. G. Muller, and P. Agostini, Observation of a train of attosecond pulses from high harmonic generation, Science **292**, 1689 (2001).

[5] A. L. Cavalieri, N. Müller, T. Uphues, V. S. Yakovlev, A. Baltuška, B. Horvath, B. Schmidt, L. Blümel, R. Holzwarth, S. Hendel, M. Drescher, U. Kleineberg, P. M. Echenique, R. Kienberger, F. Krausz, and U. Heinzmann, Attosecond spectroscopy in condensed matter, Nature (London) **449**, 1029 (2007).

[6] M. Schultze, M. Fiess, N. Karpowicz, J. Gagnon, M. Korbman, M. Hofstetter, S. Neppl, A. L. Cavalieri, Y. Komninos, T. Mercouris, C. A. Nicolaides, R. Pazourek, S. Nagele, J. Feist, J. Burgdörfer, A. M. Azzeer, R. Ernstorfer, R. Kienberger, U. Kleineberg, E. Goulielmakis *et al.*, Delay in photoemission, Science **328**, 1658 (2010).

[7] K. Klünder, J. M. Dahlström, M. Gisselbrecht, T. Fordell, M. Swoboda, D. Guénot, P. Johnsson, J. Caillat, J. Mauritsson, A. Maquet, R. Taïeb, and A. L'Huillier, Probing single-photon ionization on the attosecond time scale, Phys. Rev. Lett. **106**, 143002 (2011).

[8] A. S. Kheifets, Wigner time delay in atomic photoionization, J. Phys. B **56**, 022001 (2023).

[9] J. Dahlström, A. L'Huillier, and A. Maquet, Introduction to attosecond delays in photoionization, J. Phys. B **45**, 183001 (2012); J. Dahlström, D. Guénot, K. Klünder, M. Gisselbrecht, J. Mauritsson, A. L'Huillier, A. Maquet, and R. Taïeb, Theory of attosecond delays in laser-assisted photoionization, Chem. Phys. **414**, 53 (2013).

[10] S. Nagele, R. Pazourek, J. Feist, K. Doblhoff-Dier, C. Lemell, K. Tőkési, and J. Burgdörfer, Time-resolved photoemission by attosecond streaking: Extraction of time information, J. Phys. B **44**, 081001 (2011).

[11] S. Nagele, R. Pazourek, J. Feist, and J. Burgdörfer, Time shifts in photoemission from a fully correlated two-electron model system, Phys. Rev. A **85**, 033401 (2012).

[12] R. Pazourek, S. Nagele, and J. Burgdörfer, Attosecond chronoscopy of photoemission, Rev. Mod. Phys. **87**, 765 (2015).

[13] V. V. Serov, V. L. Derbov, and T. A. Sergeeva, in *Advanced Lasers: Laser Physics and Technology for Applied and Fundamental Science*, edited by O. Shulika and I. Sukhoivanov, Springer Series in Optical Sciences Vol. 193 (Springer, Dordrecht, 2015), pp. 213–230.

[14] U. Saalmann and J. M. Rost, Proper time delays measured by optical streaking, Phys. Rev. Lett. **125**, 113202 (2020).

[15] M. Huppert, I. Jordan, D. Baykusheva, A. von Conta, and H. J. Wörner, Attosecond delays in molecular photoionization, Phys. Rev. Lett. **117**, 093001 (2016).

[16] A. W. Bray, F. Naseem, and A. S. Kheifets, Simulation of angular-resolved RABBITT measurements in noble-gas atoms, Phys. Rev. A **97**, 063404 (2018).

[17] M. Berkane, A. Desrier, C. Lévêque, R. Taïeb, and J. Caillat, Anisotropic molecular photoemission dynamics: Wigner time delay versus time delay from RABBIT measurements, Phys. Rev. A **109**, 013101 (2024).

[18] V. Loriot, A. Boyer, S. Nandi, C. González-Collado, E. Plésiat, A. Marciniak, C. Garcia, Y. Hu, M. Lara-Astiaso, A. Palacios, P. Decleva, F. Martín, and F. Lépine, Attosecond metrology of the two-dimensional charge distribution in molecules, Nat. Phys. **20**, 765 (2024).

[19] P. Hockett, Angle-resolved RABBITT: theory and numerics, J. Phys. B **50**, 154002 (2017).

[20] J. Fuchs, N. Douguet, S. Donsa, F. Martìn, J. Burgdörfer, L. Argenti, L. Cattaneo, and U. Keller, Time delays from one-photon transitions in the continuum, Optica **7**, 154 (2020).

[21] A. Autuori, D. Platzer, M. Lejman, G. Gallician, L. Maëder, A. Covolo, L. Bosse, M. Dalui, D. Bresteau, J.-F. Hergott, O. Tcherbakoff, H. J. B. Marroux, V. Loriot, F. Lépine, L. Poisson, R. Taïeb, J. Caillat, and P. Salières, Anisotropic dynamics of two-photon ionization: An attosecond movie of photoemission, Sci. Adv. **8**, eabl7594 (2022).

[22] D. I. R. Boll, L. Martini, A. Palacios, and O. A. Fojón, Two-color polarization control of angularly resolved attosecond time delays, Phys. Rev. A **107**, 043113 (2023).

[23] S. Heuser, A. Jiménez Galán, C. Cirelli, C. Marante, M. Sabbar, R. Boge, M. Lucchini, L. Gallmann, I. Ivanov, A. S. Kheifets, J. M. Dahlström, E. Lindroth, L. Argenti, F. Martín, and U. Keller, Angular dependence of photoemission time delay in helium, Phys. Rev. A **94**, 063409 (2016).

[24] U. Fano, Propensity rules: An analytical approach, Phys. Rev. A **32**, 617 (1985).

[25] D. Busto, J. Vinbladh, S. Zhong, M. Isinger, S. Nandi, S. Maclot, P. Johnsson, M. Gisselbrecht, A. L'Huillier, E. Lindroth, and J. M. Dahlström, Fano's propensity rule in angle-resolved attosecond pump-probe photoionization, Phys. Rev. Lett. **123**, 133201 (2019).

[26] A. S. Kheifets, Symmetry analysis of the photoelectron continuum in two-photon XUV + IR ionization, Phys. Rev. A **105**, 013114 (2022).

[27] H. A. Bethe and E. E. Salpeter, *Quantum Mechanics of One- and Two-Electron Atoms* (Springer, Berlin, 1957), pp. 4–118.

[28] V. Véniard, R. Taïeb, and A. Maquet, Phase dependence of $(N+1)$-color $(N>1)$ ir-uv photoionization of atoms with higher harmonics, Phys. Rev. A **54**, 721 (1996).

[29] H. G. Muller, Reconstruction of attosecond harmonic beating by interference of two-photon transitions, Appl. Phys. B **74**, s17 (2002).

[30] M. Vacher, R. Gaillac, A. Maquet, R. Taïeb, and J. Caillat, Transition dynamics in two-photon ionisation, J. Opt. **19**, 114011 (2017).

[31] E. P. Wigner, Lower limit for the energy derivative of the scattering phase shift, Phys. Rev. **98**, 145 (1955).

[32] A. Messiah, *Quantum Mechanics* (North-Holland, Amsterdam, 1961).

[33] R. Gaillac, M. Vacher, A. Maquet, R. Taïeb, and J. Caillat, Attosecond photoemission dynamics encoded in real-valued continuum wave functions, Phys. Rev. A **93**, 013410 (2016).

[34] E. S. Toma and H. G. Muller, Calculation of matrix elements for mixed extreme-ultraviolet–infrared two-photon above-threshold ionization of argon, J. Phys. B **35**, 3435 (2002).

[35] J. Zahn, Angular time delay in quantum mechanical scattering, Phys. Scr. **98**, 085109 (2023).

[36] H. Goldstein, *Classical Mechanics* (Addison-Wesley, Reading, 1980).

[37] A. Cionga, V. Florescu, A. Maquet, and R. Taïeb, Target dressing effects in laser-assisted x-ray photoionization, Phys. Rev. A **47**, 1830 (1993).

[38] A. Maquet and R. Taïeb, Two-colour IR+XUV spectroscopies: The "soft-photon approximation", J. Mod. Opt. **54**, 1847 (2007).

[39] *Handbook of Mathematical Functions, With Formulas, Graphs, and Mathematical Tables*, Natl. Bur. Stand. (U.S.) Appl. Math.

Ser. 55, edited by M Abramowitz and I. A. Stegun (U.S. GPO, Washington, DC, 1974).

[40] E. Lindroth and J. M. Dahlström, Attosecond delays in laser-assisted photodetachment from closed-shell negative ions, Phys. Rev. A **96**, 013420 (2017).

[41] S. Saha, J. Jose, P. C. Deshmukh, G. Aravind, V. K. Dolmatov, A. S. Kheifets, and S. T. Manson, Wigner time delay in photodetachment, Phys. Rev. A **99**, 043407 (2019).

[42] C. Cirelli, C. Marante, S. Heuser, C. L. M. Petersson, Á. J. Galán, L. Argenti, S. Zhong, D. Busto, M. Isinger, S. Nandi *et al.*, Anisotropic photoemission time delays close to a Fano resonance, Nat. Commun. **9**, 955 (2018).

[43] J. Vos, L. Cattaneo, S. Patchkovskii, T. Zimmermann, C. Cirelli, M. Lucchini, A. Kheifets, A. S. Landsman, and U. Keller, Orientation-dependent stereo Wigner time delay and electron localization in a small molecule, Science **360**, 1326 (2018).

[44] R. Khademhosseini, P. C. Deshmukh, and S. T. Manson, Attosecond time delay in atomic photoionization: Angular-dependent transition from dipole to quadrupole and spin-flip dynamics, Phys. Rev. A **108**, 063107 (2023).

[45] A. Boyer, V. Loriot, S. Nandi, and F. Lépine, Probing photoionization dynamics in acetylene with angle resolved attosecond interferometry, J. Phys. Chem. A **128**, 840 (2024).

[46] D. Trabert, N. Anders, A. Geyer, M. Hofmann, M. S. Schöffler, L. P. H. Schmidt, T. Jahnke, M. Kunitski, R. Dörner, and S. Eckart, Angular dependence of the Wigner time delay upon strong-field ionization from an aligned *p* orbital, Phys. Rev. Res. **5**, 023118 (2023).